

Linear Fractional Transformation modeling of multibody dynamics around parameter-dependent equilibrium

Ervan Kassarian, Francesco Sanfedino, Daniel Alazard, Charles-Antoine Chevrier, Johan Montel

Abstract— This paper proposes a new Linear Fractional Transformation (LFT) modeling approach for uncertain Linear Parameter Varying (LPV) multibody systems with parameter-dependent equilibrium. The most common procedure relies on the polynomial fitting of a set of Linear Time Invariant models over a grid of equilibrium points, which may be time consuming and miss worst-case configurations. An alternative is the symbolic linearization of the nonlinear equations, but it is often computationally heavy for complex systems. The proposed approach relies on the linearization of the equations at the substructure level before assembly of the multibody system. The linearized model is obtained under the form of a block-diagram, from which the LFT representation can be derived as a continuous function of the uncertain, varying and design parameters. Thus, the model covers all plants within the specified bounds without introducing conservatism or fitting errors. The method can be extended to boundary conditions, bodies and kinematic joints others than those addressed in this paper by deriving their individual linearized models. Targeted engineering applications include modeling of uncertain LPV systems, robust vibrations control, robust gain scheduling, integrated control/structure co-design. Two numerical applications: gain scheduling for a LPV robotic arm, and control/structure co-design of a stratospheric balloon with on-board telescope, are proposed to illustrate the approach.

Index Terms— Multibody dynamics, Linear Fractional Transform (LFT) modeling, Linear Parameter Varying (LPV) system, robust control

NOMENCLATURE

I. INTRODUCTION

Multibody systems have applications in various fields such as aeronautics, aerospace or robotics, with numerous modeling and formulation approaches [1]. In practical engineering problems, many parameter uncertainties impact the dynamics of the system and must be taken into account for robust analysis

This work was funded by ISAE-SUPAERO and CNES (French space agency – grant 51/18660).

E. Kassarian is with ISAE-Supaero, Toulouse, 31055 France (e-mail: ervan.kassarian@isae-supaero.fr).

F. Sanfedino is with ISAE-Supaero, Toulouse, 31055 France (e-mail: francesco.sanfedino@isae-supaero.fr).

D. Alazard is with ISAE-Supaero, Toulouse, 31055 France (e-mail: daniel.alazard@isae-supaero.fr).

C.A. Chevrier is with CNES, Toulouse, 31055 France (e-mail: charlesantoine.chevrier@cnes.fr).

J. Montel is with CNES, Toulouse, 31055 France (e-mail: johan.montel@cnes.fr).

$(^*\mathbf{u})$	Skew symmetric matrix of vector \mathbf{u} , such that $\mathbf{u} \wedge \mathbf{v} = (^*\mathbf{u})\mathbf{v}$
$\frac{d\mathbf{X}}{dt} \Big _{R_x}$	Derivative of vector \mathbf{X} with respect to time in frame R_x
$[\mathbf{X}]_{R_x}$	\mathbf{X} (vector or tensor) projected in frame R_x
$\bar{\mathbf{x}}$	\mathbf{x} (scalar or vector) evaluated at equilibrium
$\frac{d}{d\cdot} \Big _{\text{eq}}$	Derivative evaluated at equilibrium
$\delta\mathbf{x}$	First-order variations of \mathbf{x} around equilibrium

and control. There are three main approaches for modeling the uncertainties of multibody systems, namely stochastic models, fuzzy set theory, and interval method, which allow to describe the uncertain parameters and solve the uncertain nonlinear equations efficiently [1]. Even though multibody dynamics are inherently nonlinear, it is often useful to linearize them at equilibrium to study the stability, perform modal analysis or apply classical linear control methods [2]. When working on the uncertain linear model, a representation of the uncertainties with a bounded and unknown operator Δ , based on the Linear Fractional Transformation (LFT), is most often preferred, as modern control theory provides powerful tools within this framework to perform worst-case robust analysis and control such as μ -analysis or \mathcal{H}_∞ synthesis [3]. Furthermore, the nonlinear system can often be approximated by a Linear Parameter Varying (LPV) model around a slowly-varying equilibrium, where the varying or nonlinear terms are also represented in the operator Δ of the LFT. LPV models are widely used for systems with varying trim conditions, such as robotic arms [4], [5], multi-body vehicles [6], [7], aircrafts [8], [9], launchers [10], [11], re-entry vehicles [12], [13], or missiles [14], [15]. However, the LFT model cannot be directly obtained when the trim point depends on uncertain or varying parameters. The use of symbolic linearization was proposed in [16]–[19] to overcome this issue, but it is computationally costly for complex systems [19], [20], especially when dealing with many parameters or high-order dynamics. Consequently, the most common practice is to perform numerical linearizations around a grid of equilibrium points corresponding to particular values of the parameters, and to generate a model covering all Linear Time Invariant (LTI) models of the grid using multivariable polynomial fitting techniques [11], [20]–[24]. However, this procedure may be time consuming, introduce fitting errors or conservatism, and miss worst-case configurations.

In the modeling of large space structures such as satellites with flexible solar panels, the trim point is generally independent from parameters. In this context, a general framework

was introduced in [25], and implemented in a generic toolbox named *Satellite Dynamics Toolbox* (SDT) [26], to build linear models of flexible multibody systems. Based on Newton-Euler equations, this tool allows to build the dynamic model of the whole structure by assembling the individual models of each substructure [27]. Some assets of this approach include the compliance with various substructure models and boundary conditions, and support of the interfacing with finite element softwares when the model includes complex substructures [28]. The approach is originally limited to tree-like structures, but it extends to closed-loop kinematic chains of flexible bodies [29]. The resulting model is provided under the form of a block-diagram with minimal number of states, and the parameters can be isolated to obtain a minimal LFT model [30], allowing robust control [31] or integrated control/structure co-design with the \mathcal{H}_∞ synthesis [32]. This framework was applied to stratospheric balloons, which can be modeled as multibody structures composed of rigid bodies connected with revolute joints [33]. These systems typically carry a telescope inside a gondola, and the pointing control must reject the pendulum-like vibrations of the structure which are governed by gravity. Therefore, the performance is sensitive to uncertainties on the masses of the bodies, which must consequently be taken into account in the control design. However, the resulting LFT model was not compliant with such uncertainties since they induce parameter-dependent trim conditions. This observation motivated the present study.

In this paper, the framework from [25]–[32] is extended to the modeling of multibody systems undergoing variations around a uniformly accelerated motion, e.g. for systems subject to gravity (robotic arms, aircrafts, civil machinery, stratospheric balloons...) or space systems during a thrust phase (launchers, spacecrafts). This specific boundary condition introduces a dependency of the trim point on parameters such as the masses or angular positions of the bodies. The proposed approach relies on the linearization of each individual substructure and kinematic joint subject to such a boundary condition, rather than resorting to symbolic trimming of the nonlinear model or polynomial fitting of a set of LTI plants. The linearized model is obtained under the form of a block diagram, and the uncertain, varying and design parameters can be isolated with a LFT representation. In particular, the model is a continuous function of all these parameters and is guaranteed to cover all plants within the specified bounds without introducing conservatism. Since the linearization procedure only relies on basic block-diagram manipulations, the LFT models can be obtained in a reasonable amount of time (less than a minute for the application examples presented in this paper). Furthermore, the proposed approach is modular, in the sense that it can be extended to other boundary conditions, bodies and kinematic joints by deriving their individual linearized models. To the authors knowledge, this approach is the first contribution addressing the parametric model linearization around parameter-dependent equilibrium in the general context of multi-body systems. Targeted engineering applications include modeling of uncertain LPV systems, robust vibrations control, prediction of worst-case configurations in preliminary design phases,

robust gain scheduling, integrated control/structure co-design.

The dynamics of rigid bodies are modeled with Newton-Euler equations in Section II. The equations of rigid connections and revolute joints are presented in Section III. In Section IV, the individual models of rigid bodies and interconnections are linearized at equilibrium. The multibody assembly procedure is detailed in Section V. Finally, Section VI presents two applications: gain scheduling for an LPV robotic arm, and control/structure co-design of a stratospheric balloon with on-board telescope.

II. RIGID BODY DYNAMICS

A. Description of the motion

Let us define a reference frame \mathcal{R} in a uniformly accelerated motion with regard to an inertial frame \mathcal{R}_i . This boundary condition can represent a gravity field or an acceleration during a thrust phase for a space system. In this paper, the motion of the system is described in the reference frame \mathcal{R} .

Definition II.1. Uniformly accelerated reference frame \mathcal{R}

Let $\mathcal{R} = (O, \mathbf{x}, \mathbf{y}, \mathbf{z})$ be a reference frame in uniform acceleration, represented with the 6×1 vector $\mathbf{a}_6 = [\mathbf{0}_{3 \times 1}^a]$ (linear and angular accelerations), with regard to an inertial frame \mathcal{R}_i .

Definition II.2. Motion in the reference frame \mathcal{R}

Let us define the following vectors:

- $\mathbf{x}_P^B = \begin{bmatrix} \overrightarrow{OP} \\ \theta^B \end{bmatrix}$ the 6×1 pose vector of body B at point P , with \overrightarrow{OP} the 3×1 position vector of P (O is the origin of \mathcal{R}) and θ^B the 3×1 vector of Euler angles of B with regard to \mathcal{R} or \mathcal{R}_i .
- $\mathbf{x}'_P^B = \begin{bmatrix} \mathbf{v}_P^B \\ \omega^B \end{bmatrix}$ the 6×1 dual velocity vector of body B at point P , with $\mathbf{v}_P^B = \frac{d\overrightarrow{OP}}{dt} \Big|_{\mathcal{R}}$ and ω^B the angular velocity of B with regard to \mathcal{R} .
- $\mathbf{x}''_P^B = \frac{d\mathbf{x}'_P^B}{dt} \Big|_{\mathcal{R}_i} = \begin{bmatrix} \dot{\mathbf{v}}_P^B \\ \dot{\omega}^B \end{bmatrix}$ the 6×1 dual acceleration vector of body B at point P .
- $\mathbf{m}_P^B = \begin{bmatrix} \mathbf{x}''_P^B \\ \mathbf{x}'_P^B \\ \mathbf{x}_P^B \end{bmatrix}$ is the 18×1 motion vector of body B at point P .

With the notations of definitions II.1 and II.2, the acceleration of body B at point P with respect to the inertial frame \mathcal{R}_i is

$$\begin{bmatrix} \mathbf{a}_P^B \Big|_{\mathcal{R}_i} \\ \dot{\omega}^B \Big|_{\mathcal{R}_i} \end{bmatrix} = \mathbf{x}''_P^B + \mathbf{a}_6 \quad (1)$$

where $\mathbf{a}_P^B \Big|_{\mathcal{R}_i}$ and $\dot{\omega}^B \Big|_{\mathcal{R}_i}$ are respectively the linear and angular accelerations of body B at point P (note that $\dot{\omega}^B$ is the same in \mathcal{R}_i and \mathcal{R}).

B. Newton-Euler equations for rigid bodies

Let us consider a body B of mass m^B and matrix of inertia \mathbf{J}_B^B at center of gravity B . Newton-Euler equations read at B :

$$\underbrace{\begin{bmatrix} \mathbf{F}^B \\ \mathbf{T}_B^B \end{bmatrix}}_{\mathbf{W}_B^B} = \underbrace{\begin{bmatrix} m^B \mathbf{I}_3 & \mathbf{0}_{3 \times 3} \\ \mathbf{0}_{3 \times 3} & \mathbf{J}_B^B \end{bmatrix}}_{\mathbf{D}_B^B} \begin{bmatrix} \mathbf{a}_P^B \Big|_{\mathcal{R}_i} \\ \dot{\omega}^B \Big|_{\mathcal{R}_i} \end{bmatrix} + \begin{bmatrix} \mathbf{0}_{3 \times 1} \\ (*\omega^B) \mathbf{J}_B^B \omega^B \end{bmatrix} \quad (2)$$

where $\mathbf{W}_B^B = \begin{bmatrix} \mathbf{F}_B^B \\ \mathbf{T}_B^B \end{bmatrix}$ is the 6×1 wrench vector (force \mathbf{F}^B and torque \mathbf{T}^B) applied to the body \mathcal{B} at point B . Definition II.3 and property II.4 were introduced in [25] to transport equation (2) to any other point P of the body \mathcal{B} .

Definition II.3. *Kinematic model [25]*

The 6×6 tensor $\tau_{PC} = \begin{bmatrix} \mathbf{I}_3 & (*\overrightarrow{PC}) \\ \mathbf{0}_{3 \times 3} & \mathbf{I}_3 \end{bmatrix}$ is defined as the kinematic model between two points P and C .

Property II.4. *Transport of the vectors [25]:*

- Dual velocity vector: $\mathbf{x}'_P^B = \tau_{PC}\mathbf{x}'_C^B$
- Dual acceleration vector:

$$\mathbf{x}''_P^B = \tau_{PC}\mathbf{x}''_C^B + \begin{bmatrix} (*\omega^B)(*\overrightarrow{PC})\omega^B \\ \mathbf{0}_{3 \times 1} \end{bmatrix}$$

- Wrench vector: $\mathbf{W}_C^B = \tau_{PC}^T \mathbf{W}_P^B$
- Inverse kinematic model: $\tau_{PC}^{-1} = \tau_{CP}$
- Transitivity: $\tau_{PC}\tau_{CP} = \tau_{PP}$.

Property II.5 directly derives from property II.4.

Property II.5. *Transport of the motion vector:*

$$\mathbf{m}_P^B = \begin{bmatrix} \mathbf{x}''_P^B \\ \mathbf{x}'_P^B \\ \mathbf{x}_P^B \end{bmatrix} = \begin{bmatrix} \tau_{PC}\mathbf{x}''_C^B + \begin{bmatrix} (*\omega^B)(*\overrightarrow{PC})\omega^B \\ \mathbf{0}_{3 \times 1} \end{bmatrix} \\ \tau_{PC}\mathbf{x}'_C^B \\ \mathbf{x}_C^B + \begin{bmatrix} \overrightarrow{CP} \\ \mathbf{0}_{3 \times 1} \end{bmatrix} \end{bmatrix}$$

Using property II.4 to transport the vectors from point B to another point P of body \mathcal{B} , and since $\tau_{BP}\mathbf{a}_6 = \mathbf{a}_6$, equation (2) is transported to P :

$$\mathbf{W}_P^B = \underbrace{\tau_{BP}^T \mathbf{D}_B^B \tau_{BP}}_{\mathbf{D}_P^B} (\mathbf{x}''_P^B + \mathbf{a}_6) + \underbrace{\begin{bmatrix} m^B (*\omega^B)(*\overrightarrow{BP})\omega^B \\ (*\omega^B)(\mathbf{J}_B^B - m^B (*\overrightarrow{BP})^2)\omega^B \end{bmatrix}}_{NL(P, \omega^B)} \quad (3)$$

where $NL(P, \omega^B)$ regroups the nonlinear terms, and \mathbf{D}_P^B is defined as the direct dynamics model of body \mathcal{B} at point P .

C. Projection in the body's frame

In order to describe each body independently from the others, equation (3) is projected in the body's reference frame \mathcal{R}_b :

$$[\mathbf{W}_P^B]_{\mathcal{R}_b} = [\mathbf{D}_P^B]_{\mathcal{R}_b} ([\mathbf{x}''_P^B]_{\mathcal{R}_b} + [\mathbf{a}_6]_{\mathcal{R}_b}) + [NL(P, \omega^B)]_{\mathcal{R}_b}. \quad (4)$$

The kinematic and direct dynamic models are conveniently written in the body's frame. The inertial uniform acceleration vector \mathbf{a} is defined in the inertial frame \mathcal{R}_i , or equivalently, in frame \mathcal{R} : $[\mathbf{a}]_{\mathcal{R}_i} = [\mathbf{a}]_{\mathcal{R}}$. With the notations of definition II.6, its projection in \mathcal{R}_b reads:

$$[\mathbf{a}]_{\mathcal{R}_b} = \mathbf{P}_{b/i}^T(\theta^B)[\mathbf{a}]_{\mathcal{R}_i}. \quad (5)$$

Definition II.6. *Direction Cosine Matrix:*

The Direction Cosine Matrix (DCM) between the body's frame $\mathcal{R}_b = (O, \mathbf{x}_b, \mathbf{y}_b, \mathbf{z}_b)$ and the frame \mathcal{R}_i , containing the coordinates of vectors \mathbf{x}_b , \mathbf{y}_b , \mathbf{z}_b expressed in frame \mathcal{R}_i , is noted $\mathbf{P}_{b/i}(\theta^B)$. The inverse function, which converts a DCM $\mathbf{P}_{b/i}$ into the equivalent Euler angles, is noted $\Theta(\mathbf{P}_{b/i}(\theta^B))$.

Definition II.7. *From Euler angle rate to angular velocity:*

The relationship between the body frame angular velocity

vector and the rate of change of Euler angles is noted $\Gamma(\theta^B)$ such that:

$$[\omega^B]_{\mathcal{R}_b} = \Gamma(\theta^B) \left. \frac{d\theta^B}{dt} \right|_{\mathcal{R}} \quad (6)$$

where $\Gamma(\theta^B)$ depends on the chosen Euler sequence [34].

III. INTERCONNECTION OF RIGID BODIES

A multi-body system can be modeled by assembling the models of individual bodies formulated in Section II. In this section, we consider two bodies \mathcal{A} and \mathcal{B} interconnected. Two types of connection are considered and represented in Fig.1: rigid connection (no relative degree of freedom), and revolute joint (one degree of freedom in rotation).

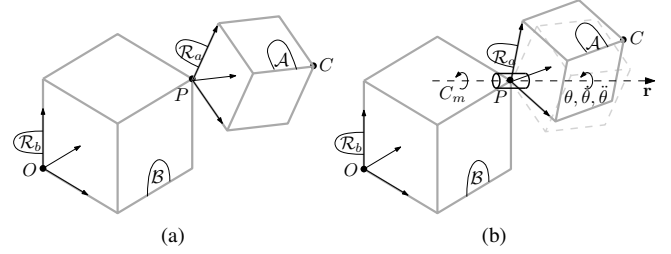


Fig. 1: Two types of interconnection between bodies the \mathcal{A} and \mathcal{B} : (a) Rigid connection, (b) Revolute joint

A. Change of frame

Since the equations describing the motion of \mathcal{B} (respectively \mathcal{A}) are projected in the reference frame \mathcal{R}_b (respectively \mathcal{R}_a), the change of frame operation is necessary to write the interconnection of \mathcal{A} and \mathcal{B} .

Property III.1. *Change of frame:*

Given the Direction Cosine Matrix (DCM) $\mathbf{P}_{a/b}$ between two frames \mathcal{R}_a and \mathcal{R}_b according to definition II.6, let us define $\mathbf{P}_{a/b}^{\times 2} = \text{diag}(\mathbf{P}_{a/b}, \mathbf{P}_{a/b})$ and $\mathbf{P}_{a/b}^{\times 18} = \text{diag}(\mathbf{P}_{a/b}^{\times 2}, \mathbf{P}_{a/b}^{\times 2}, \mathbf{P}_{a/b}, \mathbf{I}_3)$. Then:

- For X a dual velocity, acceleration, or wrench vector: $[\mathbf{X}]_{\mathcal{R}_b} = \mathbf{P}_{a/b}^{\times 2} [\mathbf{X}]_{\mathcal{R}_a}$
- Motion vector: $[\mathbf{m}_P^B]_{\mathcal{R}_b} = \mathbf{P}_{a/b}^{\times 18} [\mathbf{m}_P^B]_{\mathcal{R}_a}$
- Direct dynamics model: $\mathbf{P}_{a/b}^{\times 2} [\mathbf{D}_P^A]_{\mathcal{R}_a} \mathbf{P}_{a/b}^{\times 2 T} = [\mathbf{D}_P^A]_{\mathcal{R}_b}$
- $\mathbf{P}_{b/a} = \mathbf{P}_{a/b}^{-1} = \mathbf{P}_{a/b}^T$

B. Rigid connection

The rigid interconnection between two bodies \mathcal{A} and \mathcal{B} at point P allows no relative motion, as represented in Fig.1a. In this case, the DCM $\mathbf{P}_{a/b}$ between the reference frames \mathcal{R}_a and \mathcal{R}_b is constant. Furthermore, property III.2 addresses the transport of the motion vector from one body to another.

Property III.2. *Transformation of the motion vector through a rigid connection between two bodies:*

The motion vector at point P can be expressed from body \mathcal{B} to

body \mathcal{A} when the two bodies are rigidly interconnected at the point P . This transformation only processes the Euler angles:

$$\mathbf{m}_P^A = \begin{bmatrix} \mathbf{x}_P''^A \\ \mathbf{x}_P'^A \\ \mathbf{x}_P^A \end{bmatrix} = \begin{bmatrix} \mathbf{x}_P''^B \\ \mathbf{x}_P'^B \\ \begin{bmatrix} \vec{O}P \\ \Theta_{a/b}(\boldsymbol{\theta}^B) \end{bmatrix} \end{bmatrix}$$

where $\boldsymbol{\theta}^A = \Theta_{a/b}(\boldsymbol{\theta}^B)$ is defined as $\Theta_{a/b}(\boldsymbol{\theta}^B) = \Theta(\mathbf{P}_{b/i}(\boldsymbol{\theta}^B)\mathbf{P}_{a/b})$. Note that this function only depends on $\boldsymbol{\theta}^B$ since the DCM $\mathbf{P}_{a/b}$ is constant.

C. Connection by revolute joint

Let $\theta, \dot{\theta}, \ddot{\theta}$ be the angular configuration, rate and acceleration inside the revolute joint between bodies \mathcal{B} and \mathcal{A} at the connection point P , \mathbf{r} the vector of unit norm aligned with the joint's axis, and C_m the driving torque along \mathbf{r} , as represented in Fig.1b. The DCM $\mathbf{P}_{a/b}(\theta)$ between the reference frames \mathcal{R}_a and \mathcal{R}_b only depends on the variable θ . Furthermore, the motion vector \mathbf{m}_P^A at point P can be expressed from the motion vector \mathbf{m}_P^B at P and $\theta, \dot{\theta}, \ddot{\theta}$.

Property III.3. Transformation of the motion vector through a revolute joint between two bodies:

The motion vector at point P can be expressed from body \mathcal{B} to body \mathcal{A} when the two bodies are interconnected at the point P with a revolute joint:

$$\mathbf{m}_P^A = \begin{bmatrix} \mathbf{x}_P''^A \\ \mathbf{x}_P'^A \\ \mathbf{x}_P^A \end{bmatrix} = \begin{bmatrix} \mathbf{x}_P''^B + \ddot{\theta}\mathbf{r}_6 \\ \mathbf{x}_P'^B + \dot{\theta}\mathbf{r}_6 \\ \begin{bmatrix} \vec{O}P \\ \Theta_{a/b}^J(\boldsymbol{\theta}^B, \theta) \end{bmatrix} \end{bmatrix}$$

where $\boldsymbol{\theta}^A = \Theta_{a/b}^J(\boldsymbol{\theta}^B, \theta)$ is defined as $\Theta_{a/b}^J(\boldsymbol{\theta}^B, \theta) = \Theta(\mathbf{P}_{b/i}(\boldsymbol{\theta}^B)\mathbf{P}_{a/b}(\theta))$, and $\mathbf{r}_6 = [\mathbf{0}_{3 \times 1}^T \mathbf{r}]$.

The revolute joint \mathcal{J} is modeled as a body with two ports (it is connected to \mathcal{A} and \mathcal{B}), to which are added an input $\ddot{\theta}$ and an output C_m . It is assumed that \mathcal{J} is a mass-less body attached to the body \mathcal{A} , with a matrix of inertia $\mathbf{J}_P^J = J^J \mathbf{r} \mathbf{r}^T$. From equation (3), the dynamic model of \mathcal{J} reads:

$$\begin{aligned} \mathbf{W}_{\mathcal{B}/\mathcal{J},P} + \mathbf{W}_{\mathcal{A}/\mathcal{J},P} &= \begin{bmatrix} \mathbf{0}_3 & \mathbf{0}_3 \\ \mathbf{0}_3 & \mathbf{J}_P^J \end{bmatrix} \begin{bmatrix} \dot{\mathbf{v}}_P^A + \mathbf{a} \\ \dot{\boldsymbol{\omega}}^A \end{bmatrix} \\ &+ \begin{bmatrix} \mathbf{0}_{3 \times 1} \\ (*\boldsymbol{\omega}^A) \mathbf{J}^J \boldsymbol{\omega}^A \end{bmatrix} \\ &= \begin{bmatrix} \mathbf{0}_{3 \times 1} \\ \mathbf{J}_P^J (\dot{\boldsymbol{\omega}}^B + \ddot{\theta}\mathbf{r}) + (*\boldsymbol{\omega}^A) \mathbf{J}_P^J \boldsymbol{\omega}^A \end{bmatrix}. \end{aligned} \quad (7)$$

The driving torque C_m is the projection of the torque $\mathbf{T}_{\mathcal{B}/\mathcal{J},P}$ applied by \mathcal{B} on \mathcal{J} at P along \mathbf{r} :

$$\begin{aligned} C_m &= \mathbf{r}_6^T \mathbf{W}_{\mathcal{B}/\mathcal{J},P} \\ &= J^J (\mathbf{r}^T \dot{\boldsymbol{\omega}}^B + \ddot{\theta}) - \mathbf{r}_6^T \mathbf{W}_{\mathcal{A}/\mathcal{J},P} + \underbrace{\mathbf{r}_6^T (*\boldsymbol{\omega}^A) \mathbf{J}_P^J \boldsymbol{\omega}^A}_{=0}. \end{aligned} \quad (8)$$

In most applications, it is preferred to invert the channel from $(\theta, \dot{\theta}, \ddot{\theta})$ to C_m to take into account a driving mechanism actuating the revolute joint:

$$\ddot{\theta} = \frac{1}{J^J} (C_m + \mathbf{r}_6^T \mathbf{W}_{\mathcal{A}/\mathcal{J},P}) - \mathbf{r}^T \dot{\boldsymbol{\omega}}^B. \quad (9)$$

IV. EQUILIBRIUM AND LINEARIZATION

In this section, the equations describing the equilibrium and the linear variations around the equilibrium are derived individually for each model of rigid body, rigid connection and revolute joint obtained in Sections II and III. This procedure allows to analytically derive the parametric dependencies on simple models before assembly of the complex multibody structure.

A. Equilibrium

The system is said to be at equilibrium when it has no motion in the reference frame \mathcal{R} defined in Section II-A. For a body \mathcal{B} and a point P , it corresponds to: $\{\mathbf{x}_P^B = \bar{\mathbf{x}}_P^B, \mathbf{x}_P'^B = \mathbf{0}, \mathbf{x}_P''^B = \mathbf{0}\}$. For a revolute joint \mathcal{J} , it corresponds to $\{\theta = \bar{\theta}, \dot{\theta} = 0, \ddot{\theta} = 0\}$. The Euler angles at equilibrium are noted $\bar{\boldsymbol{\theta}}^B$. Around the equilibrium, the vectors defined in Section II-A, projected in \mathcal{R}_b , verify to the first-order:

$$\begin{cases} \delta[\mathbf{x}_P''^B]_{\mathcal{R}_b} = \frac{d(\delta[\mathbf{x}_P''^B]_{\mathcal{R}_b})}{dt} \\ \delta[\mathbf{x}_P'^B]_{\mathcal{R}_b} = \text{diag}(\mathbf{I}_3, \mathbf{\Gamma}(\bar{\boldsymbol{\theta}}^B)) \frac{d(\delta[\mathbf{x}_P^B]_{\mathcal{R}_b})}{dt} \end{cases} \quad (10)$$

where $\mathbf{\Gamma}(\boldsymbol{\theta}^B)$, from definition II.7, expresses the relation between the angular velocity vector and the rate of change of Euler angles.

B. Linearized model of the rigid body

Equation (4) is evaluated at equilibrium:

$$[\bar{\mathbf{W}}_P^B]_{\mathcal{R}_b} = [\mathbf{D}_P^B]_{\mathcal{R}_b} [\bar{\mathbf{a}}_6]_{\mathcal{R}_b} \quad (11)$$

with

$$[\bar{\mathbf{a}}_6]_{\mathcal{R}_b} = \begin{bmatrix} \mathbf{P}_{b/i}^T(\bar{\boldsymbol{\theta}}^B) [\mathbf{a}]_{R_i} \\ \mathbf{0}_{3 \times 1} \end{bmatrix}. \quad (12)$$

Equation (11) shows that the equilibrium of the system depends on the acceleration $[\mathbf{a}]_{R_i}$ and on the direct dynamics model $[\mathbf{D}_P^B]_{\mathcal{R}_b}$ of body \mathcal{B} which includes the following parameters: mass, matrix of inertia, position of the center of gravity B relatively to point P .

Equation (4) is linearized around the equilibrium:

$$\delta[\mathbf{W}_P^B]_{\mathcal{R}_b} = [\mathbf{D}_P^B]_{\mathcal{R}_b} (\delta[\mathbf{x}_P''^B]_{\mathcal{R}_b} + \delta[\mathbf{a}_6]_{\mathcal{R}_b}) \quad (13)$$

with (from equation (5)):

$$\begin{cases} \delta[\mathbf{a}_6]_{\mathcal{R}_b} = \frac{d[\mathbf{a}_6]_{\mathcal{R}_b}}{d\boldsymbol{\theta}^B} \Big|_{\text{eq}} \delta[\boldsymbol{\theta}^B]_{\mathcal{R}_b} \\ \frac{d[\mathbf{a}_6]_{\mathcal{R}_b}}{d\boldsymbol{\theta}^B} \Big|_{\text{eq}} = \frac{d}{d\boldsymbol{\theta}^B} \left(\left[\mathbf{P}_{b/i}^T(\boldsymbol{\theta}^B) [\mathbf{a}]_{R_i} \right] \right) \Big|_{\text{eq}} \end{cases}. \quad (14)$$

Then, equation (13) can be rewritten as:

$$\delta[\mathbf{W}_P^B]_{\mathcal{R}_b} = [\mathbf{D}_P^B]_{\mathcal{R}_b} \delta[\mathbf{x}_P''^B]_{\mathcal{R}_b} + [\mathbf{K}_P^B]_{\mathcal{R}_b} \delta[\mathbf{x}_P^B]_{\mathcal{R}_b} \quad (15)$$

with

$$[\mathbf{K}_P^B]_{\mathcal{R}_b} = \left[\mathbf{0}_{6 \times 3} \quad [\mathbf{D}_P^B]_{\mathcal{R}_b} \frac{d[\mathbf{a}_6]_{\mathcal{R}_b}}{d\boldsymbol{\theta}^B} \Big|_{\text{eq}} \right] \in \mathbb{R}^{6 \times 6}. \quad (16)$$

Equation (15) shows that the uniform acceleration at equilibrium introduces a stiffness, represented by the matrix $[\mathbf{K}_P^B]_{\mathcal{R}_b}$, in the linear variations of motion of body \mathcal{B} around the

equilibrium. The dynamics of these variations depend on the direct dynamics model $[\mathbf{D}_P^B]_{\mathcal{R}_b}$ and on the derivative of the projected acceleration vector at equilibrium $\left. \frac{d[\mathbf{a}_6]_{\mathcal{R}_b}}{d\theta^B} \right|_{eq}$, which, itself, depends on the Euler angles at equilibrium $\bar{\theta}^B$.

The transport of the motion vector (property II.5) can be linearized around the equilibrium:

$$\begin{cases} \delta[\mathbf{m}_P^B]_{\mathcal{R}_b} = [\mathbf{\Upsilon}_{PC}]_{\mathcal{R}_b} \delta[\mathbf{m}_C^B]_{\mathcal{R}_b} \\ [\mathbf{\Upsilon}_{PC}]_{\mathcal{R}_b} = \text{diag}([\mathbf{\tau}_{PC}]_{\mathcal{R}_b}, [\mathbf{\tau}_{PC}]_{\mathcal{R}_b}, \mathbf{I}_6) \end{cases} . \quad (17)$$

Consider a body \mathcal{B} with N ports C_i where external wrenches $\mathbf{W}_{./\mathcal{B},C_i}$ are applied respectively. From equations (10), (15), (16) and (17), the linearized 12th-order forward dynamics model at a point P is represented by the block-diagram in Fig.2a. The forward dynamics model allows to model rigid bodies when the boundary conditions are wrenches. Similarly, the linearized inverse dynamics model is represented by the block-diagram in Fig.2b. The inverse dynamics model is a static model that allows to model rigid bodies when the motion of the body is imposed as a boundary condition.

C. Linearized rigid connection

For the rigid connection, since the DCM $\mathbf{P}_{b/a}$ is constant, the linearization of the change of frame (property III.1) is straightforward. The transformation of the motion vector (property III.2), which only processes the Euler angles is linearized using:

$$\delta\theta^A = \left. \frac{d\theta_{a/b}}{d\theta^B} \right|_{eq} \delta\theta^B . \quad (18)$$

Considering that the body \mathcal{B} imposes the motion vector to the body \mathcal{A} at point P , and that \mathcal{A} applies a wrench to \mathcal{B} in return, the linearized rigid connection \mathcal{C} is represented in Fig.3.

D. Linearized model of the revolute joint

Contrary to the rigid connection, the linearization of the revolute joint must take into account the dependency of the DCM $\mathbf{P}_{a/b}$ on the variable θ : if \mathbf{X} is a vector such that $[\mathbf{X}]_{\mathcal{R}_a} = \mathbf{P}_{b/a}(\theta)[\mathbf{X}]_{\mathcal{R}_b}$:

$$\delta[\mathbf{X}]_{\mathcal{R}_a} = \mathbf{P}_{b/a}(\bar{\theta})\delta[\mathbf{X}]_{\mathcal{R}_b} + \left. \frac{d\mathbf{P}_{b/a}}{d\theta} \right|_{eq} \delta\theta [\bar{\mathbf{X}}]_{\mathcal{R}_b} . \quad (19)$$

The projections of equation (7) in the frame \mathcal{R}_b and of equation (9) along \mathbf{r} read:

$$\begin{cases} [\mathbf{W}_{\mathcal{B}/\mathcal{J},P}]_{\mathcal{R}_b} + \mathbf{P}_{a/b}^{\times 2}(\bar{\theta})[\mathbf{W}_{\mathcal{A}/\mathcal{J},P}]_{\mathcal{R}_a} \\ = \left[\begin{array}{c} \mathbf{0}_{3 \times 1} \\ [\mathbf{J}_P^{\mathcal{J}}]_{\mathcal{R}_b} ([\dot{\omega}^B]_{\mathcal{R}_b} + \ddot{\theta}[\mathbf{r}]_{\mathcal{R}_b}) + [(\ast\omega^A)\mathbf{J}_P^{\mathcal{J}}\omega^A]_{\mathcal{R}_b} \end{array} \right] \\ \ddot{\theta} = \left. \frac{1}{J^{\mathcal{J}}} (C_m + [\mathbf{r}_6^T]_{\mathcal{R}_a} [\mathbf{W}_{\mathcal{A}/\mathcal{J},P}]_{\mathcal{R}_a}) - [\mathbf{r}^T]_{\mathcal{R}_b} [\dot{\omega}^B]_{\mathcal{R}_b} \right. \end{cases} . \quad (20)$$

It can be noted that $[\mathbf{r}]_{\mathcal{R}_b}$ and $[\mathbf{J}_P^{\mathcal{J}}]_{\mathcal{R}_b}$ are independent from θ . Indeed, noting $\mathbf{R}(\theta)$ the rotation matrix around \mathbf{r} , the DCM reads $\mathbf{P}_{b/a}(\theta) = \mathbf{R}(\theta)\mathbf{P}_{b/a}(0)$. Then:

$$[\mathbf{r}]_{\mathcal{R}_b} = \mathbf{P}_{b/a}^T(0) \underbrace{\mathbf{R}^T(\theta)[\mathbf{r}]_{\mathcal{R}_a}}_{= [\mathbf{r}]_{\mathcal{R}_b}} \quad (21)$$

and

$$\begin{aligned} [\mathbf{J}_P^{\mathcal{J}}]_{\mathcal{R}_b} &= \mathbf{P}_{b/a}^T(\theta)[\mathbf{J}_P^{\mathcal{J}}]_{\mathcal{R}_a} \mathbf{P}_{b/a}(\theta) \\ &= J^{\mathcal{J}} \mathbf{P}_{b/a}^T(0) \underbrace{\mathbf{R}(\theta)^T [\mathbf{r}]_{\mathcal{R}_a}}_{= [\mathbf{r}]_{\mathcal{R}_b}} \underbrace{[\mathbf{r}^T]_{\mathcal{R}_a} \mathbf{R}(\theta)}_{= [\mathbf{r}^T]_{\mathcal{R}_b}} \mathbf{P}_{b/a}(0) \\ &= \mathbf{P}_{b/a}^T(0)[\mathbf{J}_P^{\mathcal{J}}]_{\mathcal{R}_a} \mathbf{P}_{b/a}(0) . \end{aligned} \quad (22)$$

Equation (20) is evaluated at equilibrium:

$$\begin{cases} [\bar{\mathbf{W}}_{\mathcal{J}/\mathcal{B},P}]_{\mathcal{R}_b} = \mathbf{P}_{a/b}^{\times 2}(\bar{\theta})[\bar{\mathbf{W}}_{\mathcal{A}/\mathcal{J},P}]_{\mathcal{R}_a} \\ 0 = \bar{C}_m + [\mathbf{r}_6^T]_{\mathcal{R}_a} [\bar{\mathbf{W}}_{\mathcal{A}/\mathcal{J},P}]_{\mathcal{R}_a} \end{cases} \quad (23)$$

and linearized around the equilibrium:

$$\begin{cases} \delta[\mathbf{W}_{\mathcal{B}/\mathcal{J},P}]_{\mathcal{R}_b} + \left. \frac{d\mathbf{P}_{a/b}^{\times 2}}{d\theta} \right|_{eq} [\bar{\mathbf{W}}_{\mathcal{A}/\mathcal{J},P}]_{\mathcal{R}_a} \delta\theta \\ + \mathbf{P}_{a/b}^{\times 2}(\bar{\theta})\delta[\mathbf{W}_{\mathcal{A}/\mathcal{J},P}]_{\mathcal{R}_a} \\ = \left[\begin{array}{c} \mathbf{0}_{3 \times 1} \\ [\mathbf{J}_P^{\mathcal{J}}]_{\mathcal{R}_b} (\delta[\dot{\omega}^B]_{\mathcal{R}_b} + \ddot{\theta}[\mathbf{r}]_{\mathcal{R}_b}) \end{array} \right] \\ \ddot{\theta} = \left. \frac{1}{J^{\mathcal{J}}} (\delta C_m + [\mathbf{r}_6^T]_{\mathcal{R}_a} \delta[\mathbf{W}_{\mathcal{A}/\mathcal{J},P}]_{\mathcal{R}_a}) \right. \\ \left. - [\mathbf{r}^T]_{\mathcal{R}_b} \delta[\dot{\omega}^B]_{\mathcal{R}_b} \right] \end{cases} . \quad (24)$$

Equation (23) shows that, at equilibrium, the revolute joint behaves like a rigid connection for the transfer of the wrench vector from body \mathcal{A} to body \mathcal{B} , with the driving torque C_m compensating for the wrench applied on the joint \mathcal{J} by the body \mathcal{A} . Equation (24) shows that the wrench vector at equilibrium $[\bar{\mathbf{W}}_{\mathcal{A}/\mathcal{J},P}]_{\mathcal{R}_a}$ introduces a stiffness on the motion of the revolute joint, which also depends on the angular position at equilibrium because of the matrix $\left. \frac{d\mathbf{P}_{a/b}^{\times 2}}{d\theta} \right|_{eq}$.

The change of frame (property III.1) and transformation of the motion vector (property III.3) are also linearized:

$$\begin{cases} \delta[\mathbf{x}_P^{\prime\prime A}]_{\mathcal{R}_a} = \mathbf{P}_{b/a}^{\times 2}(\bar{\theta})\delta[\mathbf{x}_P^{\prime B}]_{\mathcal{R}_b} + \delta\ddot{\theta}[\mathbf{r}_6]_{\mathcal{R}_a} \\ \delta[\mathbf{x}_P^{\prime A}]_{\mathcal{R}_a} = \mathbf{P}_{b/a}^{\times 2}(\bar{\theta})[\mathbf{x}_P^{\prime B}]_{\mathcal{R}_b} + \delta\dot{\theta}[\mathbf{r}_6]_{\mathcal{R}_a} \\ \delta[\mathbf{x}_P^A]_{\mathcal{R}_a} = \left(\begin{array}{cc} \mathbf{P}_{b/a}(\bar{\theta}) & \mathbf{0} \\ \mathbf{0} & \left. \frac{\partial\Theta_{a/b}^{\mathcal{J}}}{\partial\theta^B} \right|_{eq} \end{array} \right) \delta[\mathbf{x}_P^B]_{\mathcal{R}_b} \\ + \left(\begin{array}{c} \left. \frac{d\mathbf{P}_{b/a}}{d\theta} \right|_{eq} [\bar{\mathbf{x}}_P^B(1:3)]_{\mathcal{R}_b} \\ \left. \frac{\partial\Theta_{a/b}^{\mathcal{J}}}{\partial\theta} \right|_{eq} \end{array} \right) \delta\theta \end{cases} \quad (25)$$

where $[\bar{\mathbf{x}}_P^B(1:3)]_{\mathcal{R}_b}$ refers to the first three components of $[\bar{\mathbf{x}}_P^B]_{\mathcal{R}_b}$ (that is, the vector $[\bar{OP}]_{\mathcal{R}_b}$ at equilibrium). Based on equations (24) and (25), the 2-nd order linearized model of a revolute joint is presented by the block-diagram in Fig.4.

V. MULTIBODY ASSEMBLY PROCEDURE

Let us consider a tree-like structure with $6 + n$ degrees of freedom (DOF), composed of a parent body described by its forward dynamics (6 DOF, Fig.2.a), children bodies described by their inverse dynamics (no additional DOF, Fig.2.b), and n revolute joints (n DOF, Fig.4). Each body may be connected to any number of other bodies, as long as there is no closed kinematic loop.

Step 1 (Geometry at equilibrium): Firstly, it is required to describe the geometry of the system at equilibrium. Let

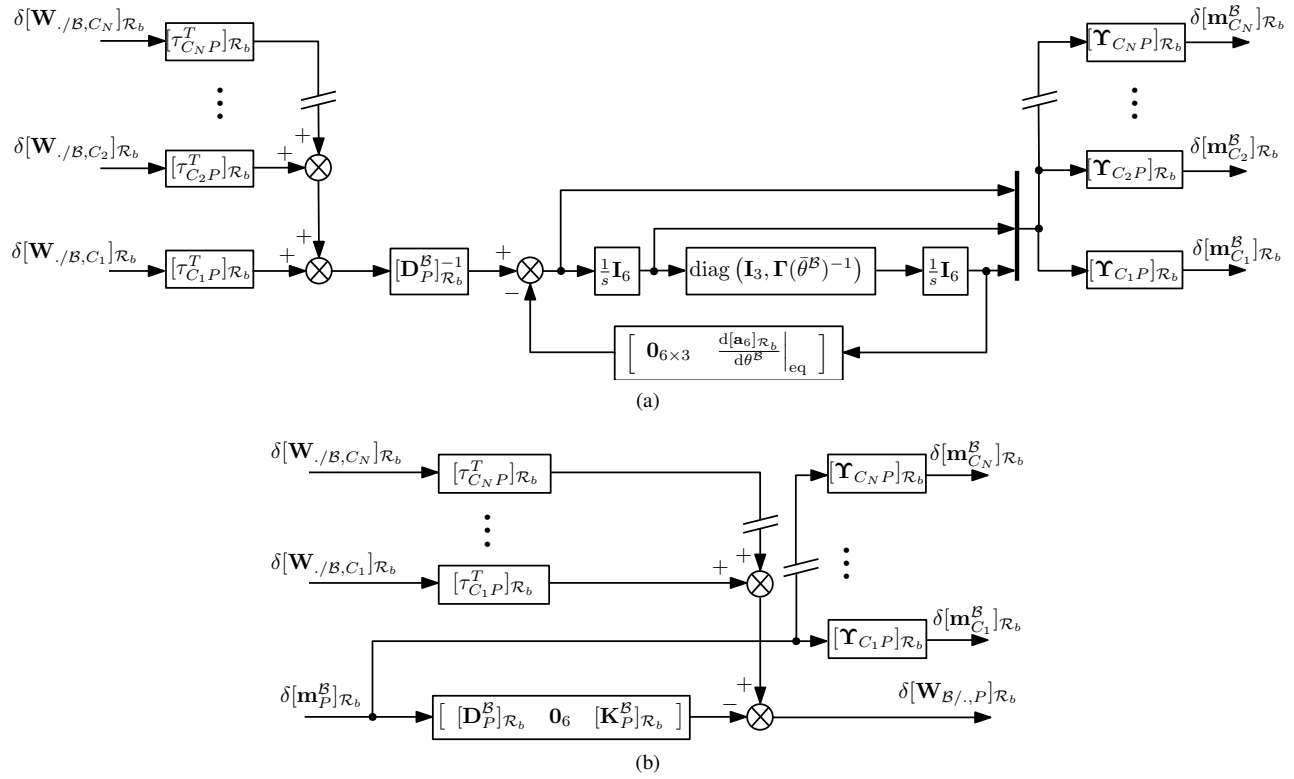


Fig. 2: Linearized model of a rigid body \mathcal{B} : (a) Forward dynamics, (b) Inverse dynamics

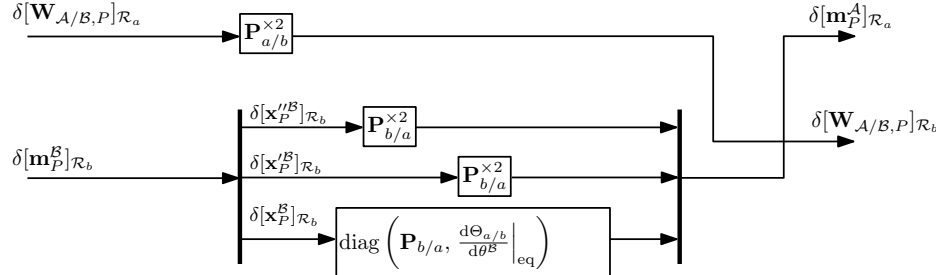


Fig. 3: Linearized model of a rigid connection \mathcal{C}

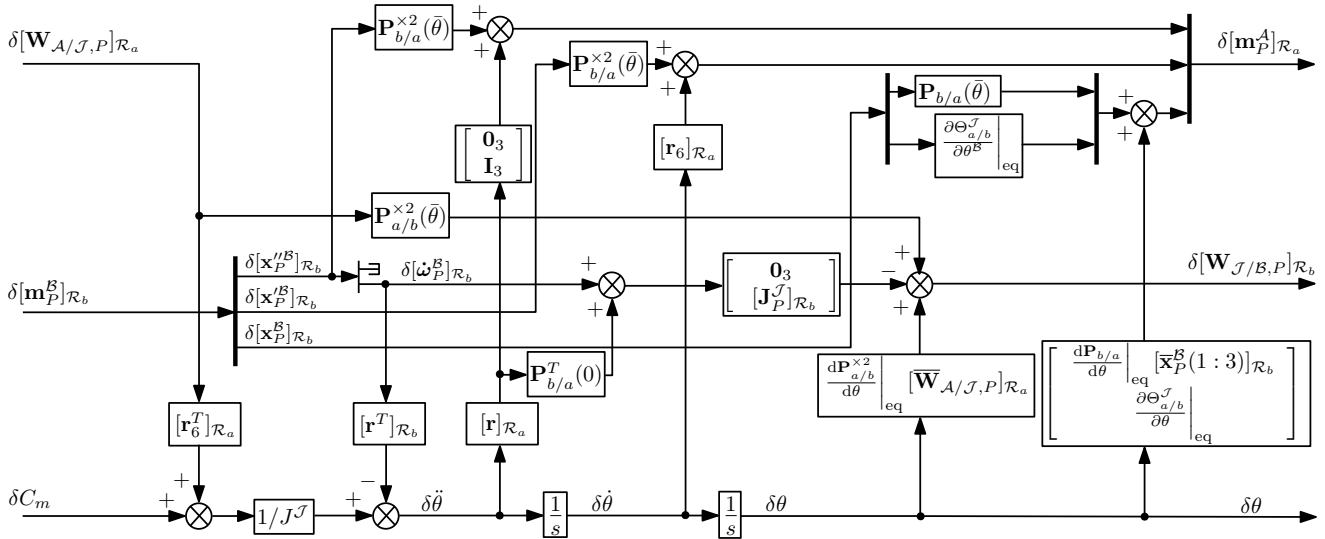


Fig. 4: Linearized model of a revolute joint \mathcal{J}

us define (i) the pose vector at one given point of the parent body at equilibrium, (ii) the angle of each revolute joint at equilibrium, and (iii) the geometry of each body (i.e. positions of the connection ports). Using the change of body properties III.2 and III.3, the Euler angles $\bar{\theta}^B$ of each body at equilibrium are determined. Using additionally the transport and reference frame change properties (respectively II.5 and III.1), the position at equilibrium of the revolute joints is determined in the adequate frame (accordingly to the notation $[\bar{x}_P^B(1:3)]_{\mathcal{R}_b}$ in Fig.4). All matrices depending on the equilibrium angles are then evaluated, namely $\Gamma(\bar{\theta}^B)$ in Fig.2, $\frac{d\Theta_{a/b}}{d\theta^B} \Big|_{eq}$ in Fig.3, and

$\mathbf{P}_{b/a}^{x2}(\bar{\theta})$, $\frac{d\mathbf{P}_{b/a}}{d\theta} \Big|_{eq}$, $\frac{\partial\Theta_{a/b}^J}{\partial\theta^B} \Big|_{eq}$ and $\frac{\partial\Theta_{a/b}^J}{\partial\theta} \Big|_{eq}$ in Fig.4. Finally,

the acceleration vector $[\bar{\mathbf{a}}]_{\mathcal{R}_b}$ and its derivative $\frac{d[\bar{\mathbf{a}}]_{\mathcal{R}_b}}{d\theta^B} \Big|_{eq}$ at equilibrium are expressed in the reference frame \mathcal{R}_b of each body B . All these quantities, which will be used as gains in the models of steps 2 and 3, can be expressed parametrically as LFT models to take into account uncertain, varying or design parameters.

Step 2 (Wrenches at equilibrium): Then, let us define (i) the external efforts applied to the bodies at equilibrium, and (ii) the direct dynamics model of each body (i.e. mass, moments of inertia and position of the center of gravity). Using additionally the acceleration vector $[\bar{\mathbf{a}}]_{\mathcal{R}_b}$ in each body's frame (derived in step 1) and the models at equilibrium (11) and (23), the wrenches applied to the revolute joints at equilibrium are derived in the adequate frame (accordingly to the notation $[\bar{\mathbf{W}}_{A/J,P}]_{\mathcal{R}_a}$ in Fig.4). Like in step 1, they can be expressed parametrically as LFT models.

Step 3 (Linearized model): Finally, the linearized models of the individual rigid bodies (Fig.2) are assembled, using either the rigid connection in Fig.3 or the revolute joint in Fig.4 to obtain a block-diagram representation from which the $2 \times (6 + n)$ -th order state-space representation can be derived (or, if the parent body is the ground, the model has order $2n$). As represented in Fig.5, the uncertain, varying and design parameters can be respectively isolated in the perturbation matrices Δ , Δ_τ and Δ_d . Although the quantities calculated in steps 1 and 2 can be expressed with minimal parametric dependency on the parameters, since they are in turn re-injected at step 3, there can be redundant occurrences in the linearized model. Thus, the blocks Δ , Δ_τ and Δ_d do not necessarily have minimal size and reduction techniques can be used to reduce the order of the LFT [35].

VI. APPLICATION EXAMPLES

In this section, two application examples are provided to show the capacities of the proposed method for the modeling and control of multibody systems with parameter-dependent trim conditions. The applications are implemented in MATLAB-SIMULINK with the *Robust control toolbox*. The uncertain and varying parameters are declared with the routine *ureal*. For each example, one SIMULINK file is created for each one of the three steps of the procedure presented in Section V by assembling the generic individual models of the bodies and connections. For steps 1 and 2, they are static

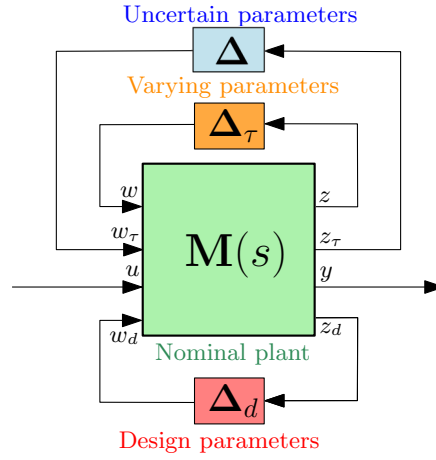


Fig. 5: LFT representation of the linearized model

models at equilibrium which allow to parametrically evaluate the quantities seen as static transfers between adequate inputs and outputs. For step 3, it is a linear dynamical model around the equilibrium from which the parametric LFT model is derived.

A. Gain scheduling for a two-link robotic arm

The two-link robotic arm presented in Fig.6 is subject to the gravity represented by the vector \mathbf{g} , which is equivalent to an acceleration $\mathbf{a} = -\mathbf{g}$ in the proposed approach. The reference frame in acceleration is noted $\mathcal{R} = (O, \mathbf{x}, \mathbf{y}, \mathbf{z})$. The arm is composed of 3 bodies B_1 , B_2 , and B_3 represented by the inverse dynamics models. The revolute joints J_1 and J_2 , which allow the rotation around \mathbf{x} , are used to connect respectively B_1 to the ground B_0 , and B_1 to B_2 . B_3 is a point mass representing the end-effector carrying a load, and is rigidly connected to B_2 . The revolute joints are actuated with torques C_{m1} and C_{m2} respectively.

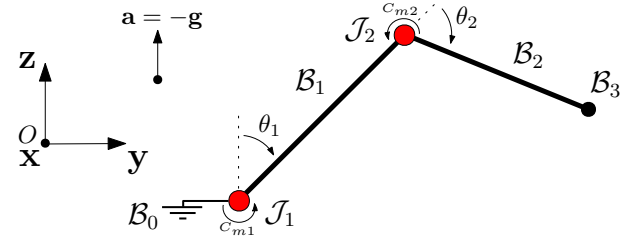


Fig. 6: Two-link robotic robotic arm

The characteristics of the rigid bodies are indicated in Table I. The position of the center of gravity (CoG) is the distance of the CoG from the connection point on the left (in Fig.6), normalized by the length of the body. Uncertainties are indicated with the mention $\pm x\%$. The moment of inertia of the shafts of the revolute joints is considered negligible, therefore it is set to 10^{-10} kg.m^2 for the numerical application. The angles belong to the following operating ranges: $\theta_1 \in [45^\circ, 90^\circ]$ and $\theta_2 \in [45^\circ, 135^\circ]$. The varying parameters $t_1 = \tan(\theta_1/2)$ and $t_2 = \tan(\theta_2/2)$ are defined, as detailed in the Appendix.

TABLE I: Characteristics of the robotic arm

	\mathcal{B}_1	\mathcal{B}_2	\mathcal{B}_3
Mass m_i (kg)	3 ($\pm 5\%$)	2	5 ($\pm 15\%$)
Moment of inertia J_i (kg.m ²)	0.2 ($\pm 10\%$)	0.1	0
Length L_i (m)	1	1 ($\pm 10\%$)	0
Position of the CoG ρ_i (-)	0.3 ($\pm 5\%$)	0.5	0

Fig. 7: Block diagram representation of the robotic arm

In this example, the varying parameters t_1 and t_2 impact the geometry of the system (step 1 of the procedure of Section V), and all parametric uncertainties defined in Table I impact the efforts at equilibrium (step 2). The block diagram representation of the linear system (step 3) is represented in Fig.7 where the blocks \mathcal{B}_i (rigid bodies), \mathcal{C} (rigid connection) and \mathcal{J}_i (revolute joints) represent the models in Fig.2b, Fig.3 and Fig.4 respectively. The linearization procedure is executed by evaluating the three SIMULINK models with the routine `ulinearize`. Then, the system is put in a LFT form where a block Δ_τ regroups the varying parameters t_1 and t_2 , and a block Δ regroups the uncertainties defined in Table I. The whole procedure (from step 1 to the LFT form) took 20 seconds on a Intel Core i7 processor. The routine `simplify`, based on [35], is called to reduce the order of the LFT. Table II shows the number of occurrences of each uncertain parameter in the model before and after the call to the routine.

TABLE II: Number of occurrences in the robotic arm model

	m_1	m_3	J_1	L_2	ρ_1	t_1	t_2
Before order reduction	5	6	1	7	5	18	24
After order reduction	3	4	1	3	2	4	10

The model is then used to tune a LPV controller to reject errors on the angles $\delta\theta_1$ and $\delta\theta_2$. The set of scheduling parameters is noted $\tau = \{t_1, t_2\}$. Noting $\delta\theta_{\text{ref}} = \begin{bmatrix} \delta\theta_1^{\text{ref}} \\ \delta\theta_2^{\text{ref}} \end{bmatrix}$ the vector of reference angles, the controller $\mathbf{K}(s, \tau)$ takes as input the vector of the angular errors $\delta\mathbf{e} = \delta\theta_{\text{ref}} - \begin{bmatrix} \delta\theta_1 \\ \delta\theta_2 \end{bmatrix}$ and produces the torque vector $\delta\mathbf{C}_m = \begin{bmatrix} \delta\mathbf{C}_m^1 \\ \delta\mathbf{C}_m^2 \end{bmatrix}$:

$$\delta\mathbf{C}_m = \mathbf{K}(s, \tau)\delta\mathbf{e}. \quad (26)$$

Let the real matrices of appropriate dimensions $\mathbf{A}(\tau)$, $\mathbf{B}(\tau)$, $\mathbf{C}(\tau)$, $\mathbf{D}(\tau)$ define the state-space representation of $\mathbf{K}(s, \tau)$. The scheduling surface $\mathbf{S}(\tau)$ is defined as a linear function of

t_1 and t_2 :

$$\mathbf{S}(\tau) = \left[\begin{array}{c|c} \mathbf{A}(\tau) & \mathbf{B}(\tau) \\ \hline \mathbf{C}(\tau) & \mathbf{D}(\tau) \end{array} \right] = \mathbf{M}_0 + \mathbf{M}_1 t_1 + \mathbf{M}_2 t_2 \quad (27)$$

where the matrices \mathbf{M}_0 , \mathbf{M}_1 , \mathbf{M}_2 are to be tuned. The controller $\mathbf{K}(s, \tau)$ reads:

$$\mathbf{K}(s, \tau) = \mathcal{F}_u \left(\mathbf{S}(\tau), \frac{\mathbf{I}_{n_s}}{s} \right) = \mathcal{F}_u (\mathbf{K}(s), \Delta_\tau^K) \quad (28)$$

where \mathcal{F}_u refers to the upper LFT, n_s is the number of states of the controller, and the block Δ_τ^K isolates the occurrences of t_1 and t_2 . The closed-loop diagram is represented in Fig.8. For simplicity, the weighting filters are chosen independent from τ , meaning that the same performances are demanded for all configurations. They are defined as: $W_r = 1$, $W_{C_m} = 1/1500$ (to limit the actuator's efforts) and $W_e(s) = \frac{s+1}{2s+0.02}$ (to penalize low-frequency tracking error).

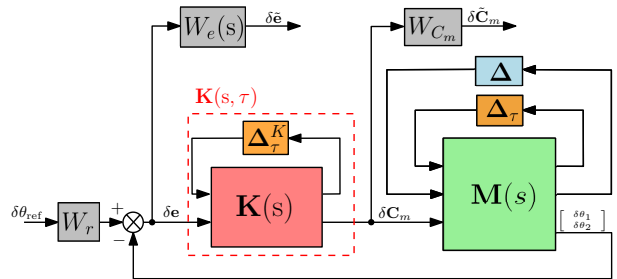


Fig. 8: Closed-loop block-diagram of the robotic arm

The value $n_s = 3$ was chosen, as it was found to yield satisfying performance for a reasonable controller complexity. The non-smooth, structured \mathcal{H}_∞ problem

$$\begin{aligned} & \text{minimize}_{\mathbf{M}_0, \mathbf{M}_1, \mathbf{M}_2} \gamma_2 \quad \text{s.t.} \quad \|\delta\theta_{\text{ref}} \rightarrow \tilde{\delta}\mathbf{C}_m\|_\infty < \gamma_2 \\ & \text{subject to:} \quad \|\delta\theta_{\text{ref}} \rightarrow \delta\mathbf{e}\|_\infty < \gamma_1 < 1 \end{aligned} \quad (29)$$

is solved with MATLAB routine `systune`, based on the algorithm presented in [36], [37], over a regular grid of size 10×10 for the scheduling parameters t_1 and t_2 . Note that, even though the LPV synthesis was performed over a grid, the open-loop and closed-loop models are defined as continuous functions of the uncertain and scheduling (varying) parameters. The μ -analysis provides an upper bound of 1.01 for γ_1 over all values of the uncertain and scheduling parameters within the specified bounds, which is satisfying and is guaranteed to include the worst-case configuration. To assess the robust performance as a function of the scheduling parameters, the model was sampled over a 30×30 grid of values of θ_1 and θ_2 , and Fig.9 shows an upper bound of the worst-case performance indices γ_1 and γ_2 computed by μ -analysis over all values of uncertain parameters defined in Table I for each fixed configuration (θ_1, θ_2) of the grid. For example, it can be seen that configurations around $(\theta_1 = 90^\circ, \theta_2 = 90^\circ)$ yield the best γ_1 performance (top plot), whereas extreme values of θ_2 within the specified bounds are the most demanding in actuator's effort (without consideration of the equilibrium torques computed at step 2), represented by the γ_2 performance (bottom plot). The Bode magnitude plot of the LPV controller $\mathbf{K}(s, \tau)$ is presented in Fig.10 for a fixed value $\theta_1 = 45^\circ$ and varying values of θ_2 .

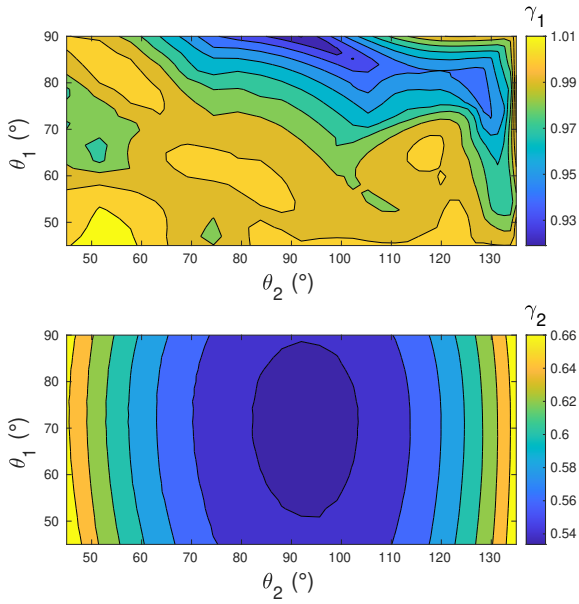


Fig. 9: Upper bound of the worst-case performance indices γ_1 and γ_2 depending on the angular configuration.

B. Integrated control/structure co-design of a stratospheric balloon with on-board telescope

Like the robotic arm, the stratospheric balloon represented in Fig.11 is subject to gravity. This application example is based on the joint NASA/CNES FIREBall experiment with simplified assumptions on the pointing system, and on the damping and disturbance models. The dynamics of the flight chain are described in [33] with a Lagrangian approach. The flight chain is a complex system that can be modeled as 11 rigid bodies, including the balloon \mathcal{B}_0 , various elements \mathcal{B}_1 to \mathcal{B}_9 , and the gondola \mathcal{B}_{10} , linked with 10 revolute joints \mathcal{J}_1 to \mathcal{J}_{10} . Inside the gondola are two additional bodies, namely the ballast \mathcal{B}_{11} (rigidly connected) and the telescope \mathcal{B}_{12} (connected with a revolute joint \mathcal{J}_{11}). The telescope is actuated at its center of gravity with a torque C_m to control the inertial line of sight, represented by the Euler angle $\theta_x^{\mathcal{B}_{12}}$ of the body 12 around \mathbf{x} with regard to frame \mathcal{R} (not represented in Fig.11). The buoyancy force \mathbf{F}_b is applied to the center of buoyancy of the balloon such that the system stays at approximately constant altitude during the pointing phase of the mission. The aerodynamic disturbance force along \mathbf{y} is noted d . It is applied to the center of pressure and, as observed in flight, it triggers the pendulum-like vibrations of the system.

The balloon is modeled with its forward dynamics model (Fig.2a), and all other rigid bodies with their inverse dynamics models (Fig.2b). However, in this example, we only consider the dynamics in the plane (\mathbf{y}, \mathbf{z}). Therefore, the unnecessary degrees of freedom of the balloon are not integrated: rotation around \mathbf{y} , rotation around \mathbf{z} , translation along \mathbf{x} , and translation along \mathbf{z} (indeed, as for a linearized pendulum, the variations of the position along \mathbf{z} are only second-order). The model order is 26. A simplified damping model is considered by adding a friction torque $C_{mi} = -K_{\mathcal{J}}\dot{\theta}_i$ with $K_{\mathcal{J}} =$

$50 \text{ N m s rad}^{-1}$ as feedback to each revolute joint \mathcal{J}_i , as well as an aerodynamic torque $T_x = -K_b\dot{\theta}_x^{\mathcal{B}_0}$ to the balloon with $K_b = 10 \text{ kN m s rad}^{-1}$. The buoyancy force \mathbf{F}_b is constant in the frame \mathcal{R} . It has direction $+\mathbf{z}$ and is equal in norm to the total weight of the system. It represents an additional boundary condition that can be expressed in the frame \mathcal{R}_{b0} of the balloon \mathcal{B}_0 the same way as the acceleration:

$$\left\{ \begin{array}{l} [\mathbf{F}_b]_{\mathcal{R}_{b0}} = \mathbf{P}_{b/i}^T(\boldsymbol{\theta}^{\mathcal{B}_0}) [\mathbf{F}_b]_{\mathcal{R}_i} \\ [\bar{\mathbf{F}}_b]_{\mathcal{R}_{b0}} = \mathbf{P}_{b/i}^T(\bar{\boldsymbol{\theta}}^{\mathcal{B}_0}) [\mathbf{F}_b]_{\mathcal{R}_i} \\ \delta[\mathbf{F}_b]_{\mathcal{R}_{b0}} = \frac{d}{d\boldsymbol{\theta}^{\mathcal{B}_0}} \left(\mathbf{P}_{b/i}^T(\boldsymbol{\theta}^{\mathcal{B}_0}) [\mathbf{F}_b]_{\mathcal{R}_i} \right) \delta\boldsymbol{\theta}^{\mathcal{B}_0} \end{array} \right. . \quad (30)$$

The uncertain and design parameters are defined as follows. The mass m_0 of the balloon (body \mathcal{B}_0) is 3231 kg with $\pm 5\%$ of uncertainty. The center of gravity (CoG) ρ_0 of the balloon is 38.4 m below the top of the balloon with $\pm 3\%$ of uncertainty, and the moment of inertia J_0 of the balloon at CoG is $5.12 \times 10^6 \text{ kg m}^2$ with $\pm 5\%$ of uncertainty. The mass of ballast (body \mathcal{B}_{11}) is considered as an uncertain parameter m_{11} ranging between 0 kg and 500 kg (ballast can be released for maneuvers in altitude throughout the flight). The moment of inertia J_{12} of the telescope (body \mathcal{B}_{12}) at CoG is 100 kg m^2 with $\pm 5\%$ of uncertainty. The moment of inertia J_{10} of the gondola (body \mathcal{B}_{10}) at CoG is 6717 kg m^2 with $\pm 5\%$ of uncertainty (independently from the uncertainty on m_{11}). It is assumed that the length l_6 of the body 6 (bifilar suspension) is a design parameter that can be adjusted between 10 m and 60 m (range imposed by operational and mechanical constraints) before the flight. The mass and moment of inertia of body 6 are calculated with parametric dependency on l_6 . The goal of this application to perform a robust control/structure co-design to perform pointing control of the line of sight: the length l_6 and a controller $K(s)$ are simultaneously tuned to minimize the actuator's efforts while ensuring robustness of the pointing performance to the uncertainties on m_0 , J_0 , ρ_0 , J_{10} and m_{11} .

In this example, the angles at equilibrium are all independent from the parameters (with value 0 for \mathcal{J}_1 to \mathcal{J}_{10} , and 40° for \mathcal{J}_{11}), so step 1 of the procedure of Section V is straightforward. However, the efforts at equilibrium (step 2) in the revolute joints \mathcal{J}_1 to \mathcal{J}_6 depend on l_6 and m_{11} , and the efforts in \mathcal{J}_7 to \mathcal{J}_{10} depend on m_{11} only. The buoyancy force (in steps 2 and 3) also parametrically depends on l_6 , m_0 and m_{11} . The parameters J_0 , ρ_0 , J_{10} and J_{12} only appear in the linear dynamics (step 3). The procedure of Section V is applied using the MATLAB-SLTUNER interface to obtain the parameterized LFT model of the system. The procedure (from step 1 to the LFT form) took 44 seconds on a Intel Core i7 processor. Table III presents the number of occurrences of each parameter in the linear model obtained at step 3. The design parameter l_6 has a complex influence on the modal frequencies and dampings of the linear model, as illustrated in Fig.12. This dependency is coupled with the parametric uncertainties (not represented in the figure). The nominal model perfectly matches the model obtained in [33] with a Lagrangian approach.

The 34-th order closed-loop model used for synthesis is presented in Fig.13, where (i) $M(s)$ is the nominal plant, (ii) the uncertain parameters m_0 , J_0 , ρ_0 , J_{10} and m_{11} are

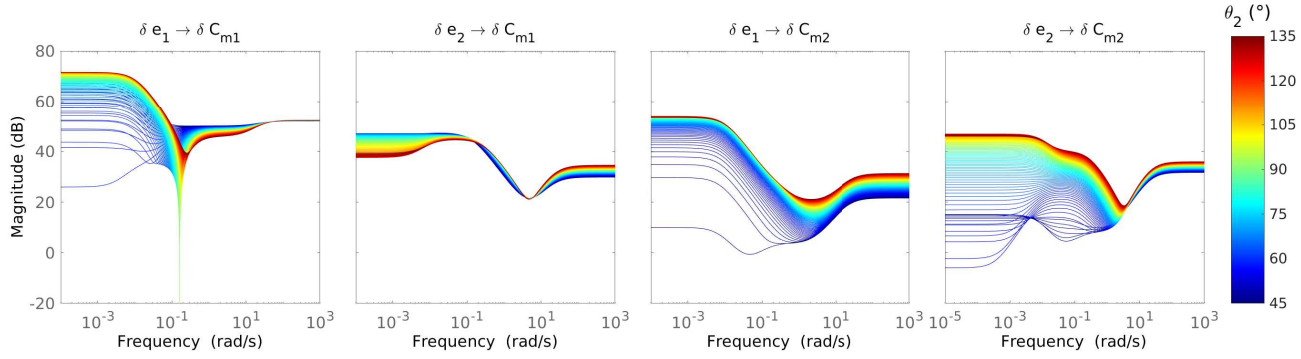


Fig. 10: LPV controller $\mathbf{K}(s, \tau)$ for the robotic arm, with $\theta_1 = 45^\circ$ and varying θ_2 .

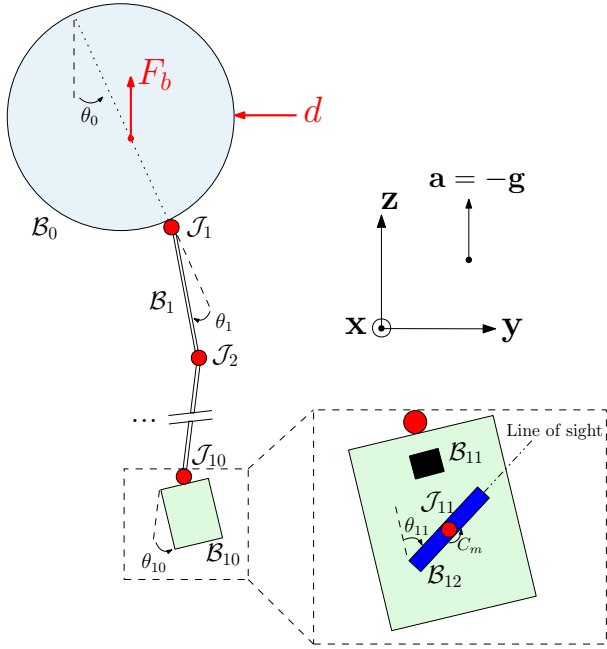


Fig. 11: Stratospheric balloon with on-board telescope

TABLE III: Number of occurrences in the balloon model

	J_0	ρ_0	m_0	l_6	J_{10}	m_{11}	J_{12}
Nb. of occurrences	1	2	2	25	1	12	1

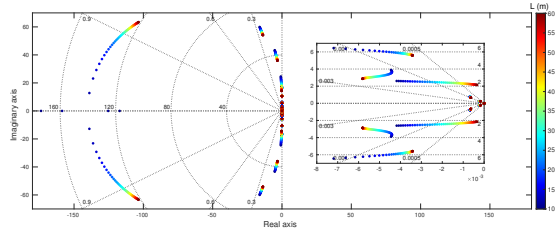


Fig. 12: Open-loop poles as a function of L , for the nominal values of the uncertain parameters

regrouped in the block Δ , (iii) the design parameter l_6 is isolated in the block $l_6\mathbf{I}_{18}$, (iv) $K(s)$ is the controller, (v)

$\tilde{K}(s)$ is the augmented controller to be tuned, (vi) $\delta\theta_{\text{ref}}$, δd , δn are respectively the reference telescope angle, aerodynamic disturbance and measurement noise, (vii) δe and δC_m are respectively the pointing error and actuator torque, (viii) $A(s) = \frac{1}{0.005s+1} \frac{-0.005s+1}{0.005s+1}$ is a model of actuator taking into account a first-order dynamic and a 10 ms delay with a first-order Padé approximation, and (ix) the weighting filters are:

$$\left\{ \begin{array}{l} W_d = \frac{130}{100s+1} , \quad W_n = \frac{9.70 \times 10^{-8}}{0.04s+1} \\ W_{e_d} = 10^5 , \quad W_{e_n} = 3.16e11 \frac{s^2+35s+625}{s^2+3500s+6.25e6} \\ W_{e_r} = \frac{0.1s+1}{0.2s+0.02} , \quad W_{C_m} = 1.78 \end{array} \right. . \quad (31)$$

The filter W_d models the frequency content of the disturbances, W_n represents the estimation noise from a gyro-stellar hybridization, W_{e_d} is the objective in disturbance rejection, W_{e_n} is the objective in noise attenuation, W_{e_r} penalizes low-frequency tracking errors, and W_{C_m} is the objective in actuator's effort.

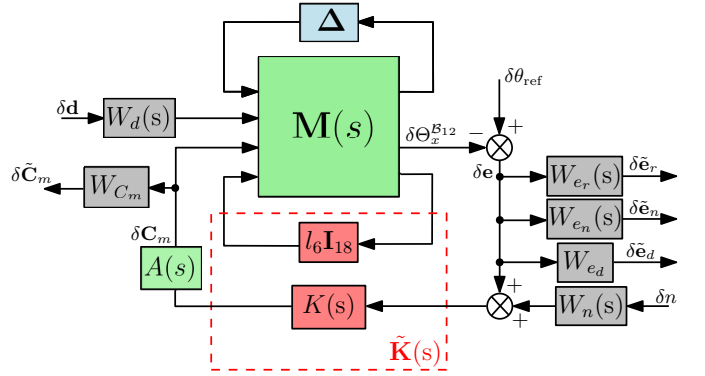


Fig. 13: Closed-loop block-diagram of the balloon

The controller is imposed to be first-order to correspond to the current FIREBall architecture. The non-smooth, structured \mathcal{H}_∞ problem

$$\begin{aligned} & \underset{\tilde{K}(s)}{\text{minimize}} \quad \gamma_4 \quad \text{s.t.} \quad \|\delta d \rightarrow \delta \tilde{C}_m\|_{\infty} < \gamma_4 \\ & \text{subject to: } \left\{ \begin{array}{l} \|\delta \theta_{\text{ref}} \rightarrow \delta \tilde{e}_r\|_{\infty} < \gamma_1 < 1 \\ \|\delta d \rightarrow \delta \tilde{e}_d\|_{\infty} < \gamma_2 < 1 \\ \|\delta n \rightarrow \delta \tilde{e}_n\|_{\infty} < \gamma_3 < 1 \end{array} \right. \end{aligned} \quad (32)$$

is again solved with *systune*. The hard requirements γ_1 , γ_2 and γ_3 are satisfied, with upper bounds of 0.98, 0.98 and 0.71 respectively. The performance objective γ_4 is reached with an upper bound of 0.93. The optimal augmented controller is composed of the length $\hat{l}_6 = 16.41$ m and of the controller $\hat{K}(s)$:

$$\hat{K}(s) = 5.24 \times 10^6 \times \frac{s + 16.75}{s + 1667} \quad (33)$$

and the robust closed-loop performances are shown in Fig.14.

VII. CONCLUSION

This paper addressed the LFT modeling of multibody systems with parameter-dependent trim point. The proposed framework takes into account the dependency of the trim point on uncertain, varying and design parameters without resorting to symbolic linearization or multi-models polynomial fitting. Thus, the resulting LFT-LPV model is a continuous function of all parameters of interest which covers all plants within the specified bounds without introducing conservatism or fitting errors. The method was developed for systems composed of rigid bodies, revolute joints, and undergoing a uniformly accelerated motion, such as systems subject to gravity or space systems during thrust phase; it can be extended to other boundary conditions, bodies and kinematic joints by deriving their individual linearized models. In the two application examples, the LFT models were obtained in less than a minute each, and were used for robust gain scheduling and robust control/structure co-design respectively.

APPENDIX

Minimal LFT of rotation matrix with varying angle

Let θ be a varying angle. The sine and cosine functions are not adequate for LFT representation since (i) they are not rational expressions in θ , and (ii) they are not independent (the relation $\cos^2(\theta) + \sin^2(\theta) = 1$ must be verified). However, let us define the new parameter $t = \tan(\theta/2)$, which varies monotonously with θ . The sine and cosine can be expressed as rational expressions in the parameter t :

$$\cos(\theta) = \frac{1 - t^2}{1 + t^2}, \quad \sin(\theta) = \frac{2t}{1 + t^2},$$

As detailed in [38], the rotation matrix

$$\mathbf{R}(\theta) = \begin{bmatrix} \cos(\theta) & -\sin(\theta) \\ \sin(\theta) & \cos(\theta) \end{bmatrix}$$

can be represented with only 2 occurrences of t . Fig.15 shows the minimal representation of $\mathbf{R}(\theta)$, with the notations $\begin{bmatrix} y_1 \\ y_2 \end{bmatrix} = \mathbf{R}(\theta) \begin{bmatrix} u_1 \\ u_2 \end{bmatrix}$.

It is also possible to define the parameter $t' = \tan(\theta/4)$ instead:

$$\cos(\theta) = \frac{(1 + t'^2)^2 - 8t'^2}{(1 + t'^2)^2}, \quad \sin(\theta) = \frac{4t'(1 - t'^2)}{(1 + t'^2)^2}$$

This choice yields more parametric occurrences (as detailed in [38], the rotation matrix can be represented with 4 occurrences of t'), but t' varies between -1 and 1 when θ varies between $-\pi$ and π (whereas t varies between $-\infty$ and $+\infty$), which is less constraining for μ -analysis tools.

REFERENCES

- [1] B. Rong, X. Rui, L. Tao, and G. Wang, "Theoretical modeling and numerical solution methods for flexible multibody system dynamics," *Nonlinear Dynamics*, vol. 98, no. 2, pp. 1519–1553, 2019.
- [2] F. González, P. Masarati, J. Cuadrado, and M. A. Naya, "Assessment of Linearization Approaches for Multibody Dynamics Formulations," *Journal of Computational and Nonlinear Dynamics*, vol. 12, no. 4, 2017.
- [3] K. Zhou, J. C. Doyle, and K. Glover, *Robust and Optimal Control*. Prentice hall, 1996.
- [4] O. Sename, D. Simon, and M. B. Gaid, "A LPV approach to control and real-time scheduling codesign: Application to a robot-arm control," *Proceedings of the IEEE Conference on Decision and Control*, pp. 4891–4897, 2008.
- [5] Z. Qiao, P. H. Nguyen, P. Polygerinos, and W. Zhang, "Dynamic modeling and motion control of a soft robotic arm segment," *Proceedings of the American Control Conference*, vol. 2019-July, pp. 5438–5443, 2019.
- [6] G. J. B. Matteo Corno, Sergio M. Savarese, "On linear-parameter-varying (LPV) slip-controller design for two-wheeled vehicles," *International Journal of Robust and Nonlinear Control*, 2008.
- [7] C. Poussot, A. Drivet, O. Sename, L. Dugard, and R. A. Ramírez-Mendoza, "A self tuning suspension controller for multi-body quarter vehicle model," in *IFAC Proceedings Volumes (IFAC-PapersOnline)*, vol. 17, 2008, pp. 3410–3415.
- [8] A. Hjartarson, P. Seiler, and G. J. Balas, "LPV analysis of a gain scheduled control for an aeroelastic aircraft," *Proceedings of the American Control Conference*, pp. 3778–3783, 2014.
- [9] C. Poussot-Vassal and C. Roos, "Generation of a reduced-order LPV/LFT model from a set of large-scale MIMO LTI flexible aircraft models," *Control Engineering Practice*, vol. 20, no. 9, pp. 919–930, 2012. [Online]. Available: <http://dx.doi.org/10.1016/j.conengprac.2012.06.001>
- [10] A. Marcos, S. Bennani, C. Roux, and M. Valli, "LPV modeling and LFT uncertainty identification for robust analysis: Application to the VEGA launcher during atmospheric phase," *IFAC-PapersOnLine*, vol. 48, no. 26, pp. 115–120, 2015.
- [11] D. Navarro-Tapia, A. Marcos, S. Bennani, and C. Roux, "Linear Parameter Varying Control Synthesis for the atmospheric phase VEGA launcher*," *IFAC-PapersOnLine*, vol. 51, no. 26, pp. 68–73, 2018.
- [12] A. Oharat, Y. Yamaguchi, and T. Morito, "LPV modeling and gain scheduled control of re-entry vehicle in approach and landing phase," in *AIAA Guidance, Navigation, and Control Conference and Exhibit*, no. August, 2001.
- [13] A. Marcos, J. Veenman, C. Scherer, G. De Zaicom, D. Mostaza, M. Kerr, H. Körögölu, and S. Bennani, "Application of LPV modeling, design and analysis methods to a re-entry vehicle," in *AIAA Guidance, Navigation, and Control Conference*, 2010, pp. 1–18.
- [14] W. Tan, A. K. Packard, and G. J. Balas, "Quasi-LPV Modeling and LPV Control of a Generic Missile," in *American Control Conference*, Chicago, Illinois, 2000.
- [15] P. C. Pella, P. Apkarian, and H. D. Tuan, "Missile autopilot design via a multi-channel LFT/LPV control method," *International Journal of Robust and Nonlinear Control*, vol. 12, no. 1, pp. 1–20, 2002.
- [16] A. Marcos, D. G. Bates, and I. Postlethwaite, "Exact nonlinear modelling using symbolic linear fractional transformations," *IFAC Proceedings Volumes (IFAC-PapersOnline)*, vol. 16, pp. 190–195, 2005.
- [17] C. Döll, C. Berard, A. Knauf, and J. M. Biannic, "LFT modelling of the 2-DOF longitudinal nonlinear aircraft behaviour," *Proceedings of the IEEE International Symposium on Computer-Aided Control System Design*, vol. 33, no. 0, pp. 864–869, 2008.
- [18] J. P. Dijkgraaf and S. Bennani, "Low order LFT modelling and generation from the non-linear equations of motion for a fighter aircraft," *2002 IEEE International Symposium on Computer Aided Control System Design, CACSD 2002 - Proceedings*, pp. 236–241, 2002.
- [19] Z. Szabó, A. Marcos, D. Mostaza Prieto, M. L. Kerr, G. Rödönyi, J. Bokor, and S. Bennani, "Development of an integrated LPV/LFT framework: Modeling and data-based validation tool," *IEEE Transactions on Control Systems Technology*, vol. 19, no. 1, pp. 104–117, 2011.
- [20] A. Varga, G. Looye, D. Moermann, and G. Grubel, "Automated generation of LFT-based parametric uncertainty descriptions from generic aircraft models," *Mathematical and Computer Modelling of Dynamical Systems*, vol. 4, no. 4, pp. 249–274, 1998.
- [21] H. Pfifer and S. Hecker, "Generation of optimal linear parametric models for LFT-based robust stability analysis and control design," *IEEE Transactions on Control Systems Technology*, vol. 19, no. 1, pp. 118–131, 2011.

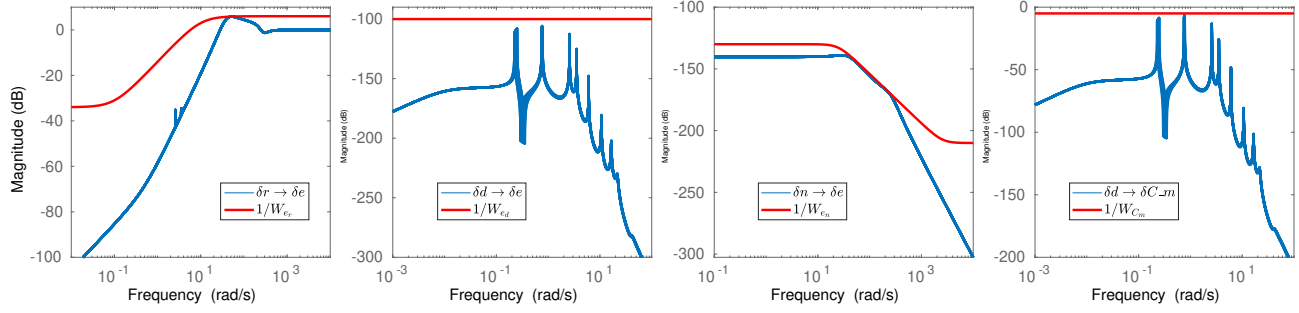


Fig. 14: Robust closed-loop performance of the co-design for the stratospheric balloon (500 samples)

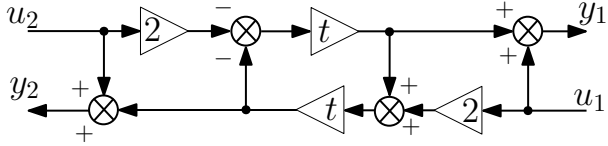


Fig. 15: Block-diagram representation of $\mathbf{R}(\theta)$ with minimal repetition of $t = \tan(\theta/2)$, from [38].

- [22] H. Hindi, C. Y. Seong, and S. Boyd, “Computing optimal uncertainty models from frequency domain data,” *Proceedings of the IEEE Conference on Decision and Control*, vol. 3, no. December, pp. 2898–2905, 2002.
- [23] A. Iannelli, P. Simplício, D. Navarro-Tapia, and A. Marcos, “LFT Modeling and μ Analysis of the Aircraft Landing Benchmark,” *IFAC-PapersOnLine*, vol. 50, no. 1, pp. 3965–3970, 2017.
- [24] C. Roos, G. Hardier, and J. M. Biannic, “Polynomial and rational approximation with the APRICOT Library of the SMAC toolbox,” *2014 IEEE Conference on Control Applications, CCA 2014*, pp. 1473–1478, 2014.
- [25] D. Alazard, C. Cumer, and K. Tantawi, “Linear dynamic modeling of spacecraft with various flexible appendages and on-board angular momentums,” *7th International ESA Conference on Guidance, Navigation and Control Systems*, vol. 41, no. 2, pp. 11 148–11 153, 2008.
- [26] D. Alazard and F. Sanfedino, “Satellite Dynamics Toolbox for Preliminary Design Phase,” *43rd Annual AAS Guidance and Control Conference*, vol. 172, pp. 1461–147, 2020.
- [27] D. Alazard, J. A. Perez, T. Loquen, and C. Cumer, “Two-input two-output port model for mechanical systems,” in *AIAA Guidance, Navigation, and Control Conference, 2013*. Reston, Virginia: American Institute of Aeronautics and Astronautics, jan 2015.
- [28] F. Sanfedino, D. Alazard, V. Pommier-Budinger, A. Falcoz, and F. Boquet, “Finite element based N-Port model for preliminary design of multibody systems,” *Journal of Sound and Vibration*, vol. 415, pp. 128–146, 2018.
- [29] J. Chebbi, V. Dubanchet, J. A. Perez Gonzalez, and D. Alazard, “Linear dynamics of flexible multibody systems: A system-based approach,” *Multibody System Dynamics*, vol. 41, no. 1, pp. 75–100, 2017.
- [30] N. Guy, D. Alazard, C. Cumer, and C. Charbonnel, “Dynamic Modeling and Analysis of Spacecraft With Variable Tilt of Flexible Appendages,” *Journal of Dynamic Systems, Measurement, and Control*, vol. 136, no. 2, 2014.
- [31] F. Sanfedino, V. Preda, V. Pommier-Budinger, D. Alazard, F. Boquet, and S. Bennani, “Robust Active Mirror Control Based on Hybrid Sensing for Spacecraft Line-of-Sight Stabilization,” *IEEE Transactions on Control Systems Technology*, vol. 29, no. 1, pp. 220–235, 2021.
- [32] J. A. Perez, C. Pittet, D. Alazard, and T. Loquen, “Integrated Control/Structure Design of a Large Space Structure using Structured Hinfinity Control,” *IFAC-PapersOnLine*, vol. 49, no. 17, pp. 302–307, 2016.
- [33] E. Kassarian, F. Sanfedino, D. Alazard, H. Evain, and J. Montel, “Mod-

eling and stability of balloon-borne gondolas with coupled pendulum-torsion dynamics,” *Aerospace Science and Technology*, vol. 112, p. 106607, 2021.

- [34] P. Zipfel, *Modeling and Simulation of Aerospace Vehicle Dynamics*, ser. AIAA education series. American Institute of Aeronautics and Astronautics, 2014.
- [35] A. Varga and G. Looye, “Symbolic and numerical software tools for LFT-based low order uncertainty modeling,” *Proceedings of the IEEE International Symposium on Computer-Aided Control System Design*, no. 1, pp. 1–6, 1999.
- [36] P. Apkarian, “Tuning controllers against multiple design requirements.” *Proceedings of the American Control Conference*, pp. 3888–3893, 2013.
- [37] P. Apkarian, M. N. Dao, and D. Noll, “Parametric Robust Structured Control Design,” *IEEE Transactions on Automatic Control*, vol. 60, no. 7, pp. 1857–1869, 2015.
- [38] V. Dubanchet, “Modeling and Control of a Flexible Space Robot to Capture a Tumbling Debris,” Ph.D. dissertation, Ecole Polytechnique de Montréal, 2016.